

Performance of Avocado Seeds as New Green Corrosion Inhibitor for 7075-T6 Al Alloy in a 3.5% NaCl Solution: Electrochemical, Thermodynamic, Surface and Theoretical Investigations

M. Radi^{1*}, R. Melian¹, M. Galai^{1*}, N. Dkhirche¹,
E. Ech-chihbi² and M. Ebn Touhami¹

¹Advanced Materials and Process Engineering Laboratory, Faculty of Science,
Ibn Tofail University, P. O. Box 133-14000 Kenitra, Morocco

²Laboratory of Organometallic, Molecular Materials and Environment, Faculty of
Science, Sidi Mohamed Ben Abdellah University, P. O. Box 1796, Fez, Morocco

*Corresponding authors: galaimouhsine@gmail.com / radi.morad@gmail.com

Received 28/01/2022; accepted 30/05/2022
<https://doi.org/10.4152/pea.2023410603>

Abstract

AS inhibition effect on the corrosion behavior of AA in a 3.5% NaCl solution was herein studied using electrochemical, thermodynamic, surface analysis and DFT (B-3LYP, at 6-31G (d, p)) techniques. The obtained results showed that AS inhibited AA corrosion process. Maximum IE(%) of around 85% was reached with AS C of 1 g/L, and it was stable as T increased from 298 to 328 K. Furthermore, AS acted as a mixed-type inhibitor through electrostatic interaction (physical adsorption), which was more dominant than chemical adsorption, between the charged molecules and the AA surface. EIS measurements confirmed these results. SEM coupled with EDX showed that AS were preferentially adsorbed onto the AA surface. AFM results demonstrated that R_a values were reduced from 338 μm to 79 nm. X-RD offered suitable support to PDP and EIS studies. There was an excellent agreement between experimental and computed data. Pc effectiveness was investigated by DFT studies, having followed the order: GA > D-M.

Keywords: 3.5% NaCl, AA, AFM, AS, DFT, EDX, EIS, corrosion, IE(%), PDP, SEM and X-RD.

Introduction*

AA 7000 series (Al-Zn-Mg), with 7075-T6 at the head, are widely used for structural parts, due to their excellent mechanical properties/weight ratio and manufacturing cost. However, these alloys are likely to be affected by the corrosion phenomenon, mostly localized, mainly due to intermetallic particles of different compositions, which cause the creation of new phases with electrochemical properties very different from those of the Al matrix. These particles, such as Mg_2Si , MgZn_2 , $\text{Al}_7\text{Cu}_2\text{Fe}$, Al_2CuMg , Al_2Cu and Al_3Fe , promote micro-coupling, which is often the main cause of localized corrosion [1-4]. The metallic surface is energetically heterogeneous, due to local disordering. The

* The abbreviations and symbols definition lists are in pages 441-442.

particles that are anodic, concerning the matrix, tend to dissolve. The particles that are cathodic promote the matrix dissolution. Cu and Fe are more cathodic than the Al matrix, which causes galvanic corrosion.

The combination of different layers helps protect materials against corrosion in a sustainable way. However, when damage is initiated, the coatings can no longer protect the bare metal. Corrosion inhibitors are substances that decrease metals reaction with their environment, when added at low C to corrosive media. An inhibitor can function by adsorption onto the metal surface, thus reducing CR.

Most synthetic inhibitors have good corrosion inhibiting properties, but their majority are toxic to the environment, and can cause temporary or permanent damage to organs, such as the kidneys or the liver, or disrupt the body enzyme system. Therefore, due to environmental concerns, plants are increasingly seen as a source of green corrosion inhibitors. They are used to protect metals and alloys from aggressive environments, replacing toxic chemicals. Several studies on the development of green inhibitors have been carried out for application in the protection of metals and alloys against corrosion [5-7]. Avocado (*Persea Americana*) belongs to the *Lauraceae* family. AS have many health benefits, due to their composition [8]. They are considered a natural source of proteins, antioxidants, vitamins (B1, B2, B3, C, A and E), minerals (P, Ca, Zn, Na, Fe, K and Cu) polyunsaturated fatty acids and trace elements [9].

The present study aimed to research and exploit a natural inhibitor for the corrosion inhibition of AA, in 3.5% NaCl, used in the aeronautical industry. Compared to IE(%) values of other inhibitors, such as *Phoenix dactylifera L.* (63%) [10], plant-derived cationic dye (78%) [11] and Berberine (80%) [12], those obtained in this work have reached satisfactory values.

Experimental part

Inhibitor preparation

AS were washed for eliminating impurities, dried at 50 °C, in order to prevent deterioration of physical and chemical properties, and, then, powdered by grinding. The powder was sifted and analyzed by FTIR.

The samples FTIR spectra were recorded with a VERTEX 70 device, at the wavelength range from 400 to 4000 cm^{-1} , in ATR mode. The powder was pelletized at about 1% by wt. in KBr previously stored in an oven at 100 °C, and under a pressure of about 1000 psi.

Materials and solutions

A conventional electrochemical cell with three electrodes was used. The WW (AA) had an area of 1cm^2 , and it was prepared by grinding abrasive paper (gradation from 220 to 2000). Ag/AgCl (3 M C in Cl) were used as RE, while Pt was the CE. Then, the samples were rinsed and degreased with acetone. Before each analysis, they were immersed in an electrochemical cell and stabilized for 2 h. AS easily dissolved with distilled water, at ambient T. AS C of 0.25, 0.5, 0.75 and 1 g/L were prepared in a 3.5% NaCl solution. AA had the following composition (wt%): Zn (5.81), Mg (2.62), Cu (1.59), Cr (0.19), Mn (0.01), Ti (0.02), Si (0.08), Fe (0.23) and Al (balance).

Polarization measurements

The WW was immersed in the solution for 2 h, until E_{ocp} was constant, as a function of time. The cathodic polarization curve was registered from E_{ocp} towards the negative direction, with a SR of 1 mV/s.

After this scan, the same electrode remained in the solution until E_{corr} steady state ($E_{ocp} \pm 0.02$ V) was achieved. Afterwards, the anodic polarization curve was registered from E_{ocp} towards the anodic domain, with the same scanning speed. These measurements were done utilizing a PGZ100 potentiostat, controlled by a PC. For each essay, three independent experiments were performed.

The Tafel extrapolation method of the linear cathodic domain was utilized to extract the corrosion kinetic parameters. IE(%) was extracted from i_{corr} values, using the following equation:

$$\eta = \frac{i_{corr}^0 - i_{corr}}{i_{corr}^0} \times 100 \quad (1)$$

where i_{corr}^0 and i_{corr} are values in AS absence and presence, respectively.

EIS measurements

EIS was performed employing a transfer function analyzer (Voltalab PGZ 100, Radiometer Analytical) over the frequency range from 100 kHz to 0,01 Hz, with 10 points per decade. The applied amplitude of the AC signal was 30 mV. All experiments were performed at the circuit E. The obtained impedance data were investigated within the equivalent circuit, using Bouckamp's program [13]. IE(%) was evaluated from R_p values by:

$$IE(\%) = \frac{R_p - R_p^0}{R_p} \times 100 \quad (2)$$

where R_p^0 and R_p represent values in AS absence and presence, respectively.

Surface study

Using a SEM model (JOEL JSM-5500), micrographs of the corroded and protected AA surfaces were obtained. The samples surface R_a was measured with an AFM (Nano Surf), in non-contact mode, and the images were processed using Gwyddion software. AA surfaces were examined using X-RD X'Pert Pro MPD model.

Computational study

DFT calculations

AS major constituents are GA and D-M. The two major molecules were optimized by utilizing DFT-B3LYB method. B3LYP and 6-31G (d, p) basis set, operated with Gaussian 09 software, were used in gas and aqueous media. The solvation model using IEFPCM was also employed to examine the water molecules solvent effect. For the considered AS molecules, E_{HOMO} , E_{LUMO} , ΔE , η , χ and ΔN were computed. Quantum chemical descriptors were determined according to the following equations [14,15]:

$$\Delta E_{gap} = E_{LUMO} - E_{HOMO} \quad (3)$$

$$\eta = \frac{\Delta E_{gap}}{2} = \frac{(E_{LUMO} - E_{HOMO})}{2} \quad (4)$$

$$\sigma = \frac{1}{\eta} = \frac{2}{E_{LUMO} - E_{HOMO}} \quad (5)$$

$$\Delta N = \frac{\Phi - \chi_{inh}}{2(\eta_{Fe_{10}} + \eta_{inh})} \quad (6)$$

According to Pearson, ϕ and η are equal to 4.82 and 0 eV, respectively. Fukui indices are useful predictors of reactive sites for nucleophilic and electrophilic attacks [16, 17].

$$f_k^+ = P_k(N+1) - P_k(N) \text{ for nucleophilic attack} \quad (7)$$

$$f_k^- = P_k(N) - P_k(N-1) \text{ for electrophilic attack} \quad (8)$$

where $P_k(N)$, $P_k(N+1)$ and $P_k(N-1)$ are the molecule neutron, anion and cation, respectively. MPA was used to express Fukui functions in the present study.

Results and discussion

AS characterization and chemical composition

Fig. 1 shows AS vibration bands.

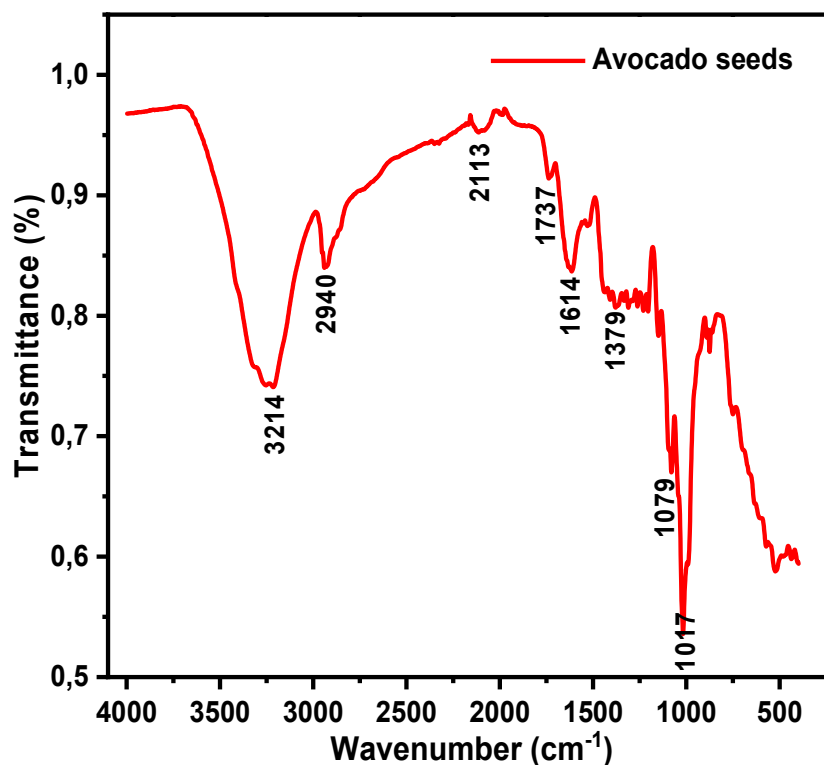


Figure 1. AS IR spectra.

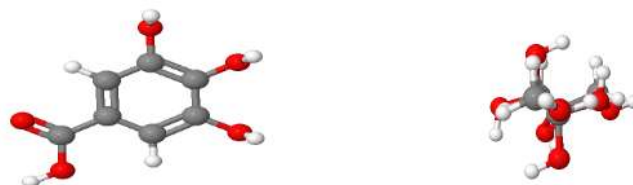
Spectra data for AS FTIR are presented in Table 1.

Table 1. Most characteristic AS IR bands.

Wave number cm ⁻¹	Bond	Intensity
3214	$\nu O-H$	0.74
2940	$\nu C-H$	0.84
2113	$C \equiv C$	0.95
1737	$\nu C-C$	0.91
1614	$\nu c=c$	0.83
1379	$\delta s(CH_3)$	0.80
1079	C-O	0.67
1017	$\nu O-H$	0.53

AS IR spectra are presented in Fig. 1. IR peaks of O–H (3214 cm⁻¹) vibrations were identified. IR band at 2940 cm⁻¹ was attributed to the C–H stretching vibration, and the 2113 cm⁻¹ absorption band is characteristic of C≡C stretching vibrations. In addition, a vibration band at 1614 cm⁻¹ was attributed to C=C, and the absorption band at 1079 cm⁻¹ is characteristic of C–O stretching vibrations. Regarding AS extract chemical composition, [18] reported that it is essentially composed of 10% GA and 5% D-M, which represents 90% of the inhibitor.

GA and D-M chemical compositions are presented in Fig. 2. These major AS compounds contain C–O, C=C, C–H and O–H groups, all of which have been identified by FTIR spectroscopy.

**Figure 2.** GA and D-M chemical composition.

Electrochemical measurements

PDP measurements

PDP measurements were carried out in a large E domain, in order to study AS effect on the partial anodic and cathodic reactions, at a SR of 1 mV/s.

Fig. 3 shows the polarization curve for AA in a 3.5% NaCl solution without and with AS, at different C (0.25, 0.5, 0.75 and 1 g/L).

In AS absence, the curve is characterized by different electrochemical reactions. On the anodic side, the branch is characterized by a strong increase in J, due to the propagation of galvanic and pitting corrosion localized on the AA surface (eq. 9). On the cathodic side, the plateau observed is associated with dissolved O reduction in the solution (eq. 10). The limiting J is in the order of 10⁻¹ mA/cm⁻². The increase in J for the lowest cathodic E corresponds to the water reduction reaction (eq. 11).



In AS presence, the anodic branch was characterized by a wide plateau of 320 mV, with a slightly positive slope, suggesting that the alloy was probably not in the passive state, but rather covered with a very protective film.

On the cathodic side, J associated with dissolved O reduction was decreased by almost two decades, compared to the reference. This strong decrease was due to the formation of a passive film on the matrix, which provided a pronounced barrier effect that limited O reduction on the intermetallic particles [19-21].

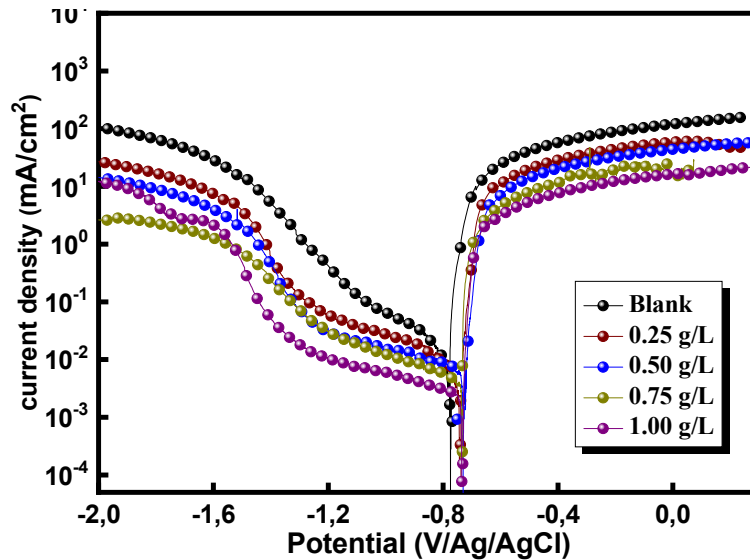


Figure 3. Polarization curves for AA without and with AS, in various C, after 2 h of immersion, at 298 K. The scan rate is $|dE/dt| = 1 \text{ mV/s}^{-1}$.

Table 2 presents electrochemical parameters: E_{corr} , i_{corr} , β_c and $IE(\%)$. Tafel extrapolation method of the linear cathodic part, in both AS absence and presence, was used. $IE(\%)$ was obtained from the relation in Eq (1).

Table 2. Electrochemical parameters for AA in 3.5% NaCl containing various AS C, at 298 K.

C g/L	E_{corr} mV/Ag/AgCl	i_{corr} $\mu\text{A cm}^{-2}$	$-\beta_c$ mV/dec ⁻¹	IE(%)
Blank	774±0.1	10.8±0.3	359±1	-
0.25	735±0.4	6.8±0.1	298±4	37.0
0.50	729±0.6	5.5±0.2	295±2	49.0
0.75	730±0.2	5.2±0.5	290±5	51.8
1.00	733±0.1	1.4±0.1	293±1	87.0

The results reported in Table 2 show that i_{corr} decrease as AS C increased. The same is true for CR. $IE(\%)$ reached a maximum value of about 87% at 1 g/L AS. This is related to the low recorded i_{corr} , which was about $1.4 \mu\text{A/cm}^2$. AS addition slightly modified E_{corr} values. Compared to other inhibitors, such as *Phoenix dactylifera L.* (63%) [10] and plant-derived cationic dye (78%) [11], AS $IE(\%)$ obtained during this study was significant, improving the protection against AA corrosion.

EIS

EIS diagrams obtained at OCP of AA, after 2 h immersion in 3.5% NaCl without and with AS, at 298 ± 2 K, are shown in Fig. 4. These diagrams were obtained after E_{corr} was stable, which allowed for a well-defined low-frequency of the diagram.

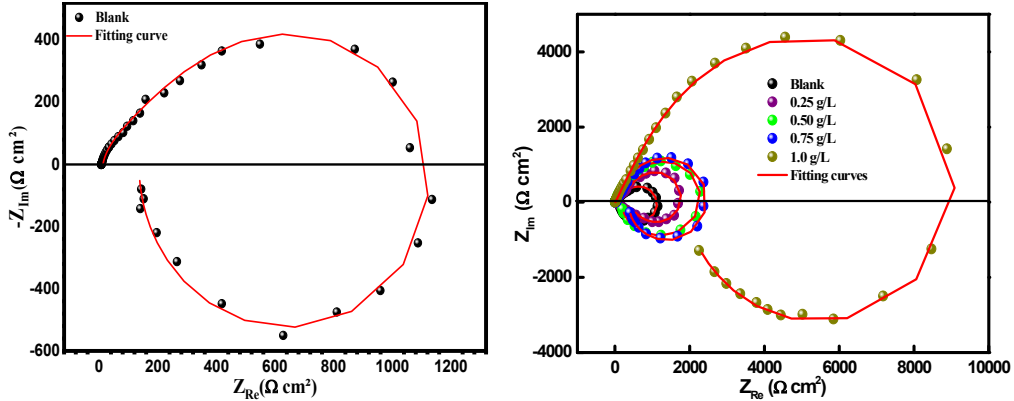


Figure 4. Nyquist plots of AA without and with different C of AS in 3.5% NaCl.

EIS diagrams, in the complex plane depiction of the Nyquist diagram presented in Fig. 4, are characterized by capacitive loops in the high and medium frequencies. The first capacitive loop is the load transfer resistance, which is parallel to the high-frequency capacitor, while the second one, at the medium frequency region, was originated from the formed oxide film.

The impedance diagrams also show an inductive loop at low frequencies. However, according to the work of [22-24], an inductive loop can be obtained under certain conditions, if the overall reaction consists of two electrochemical reactions involving an adsorbed intermediate. Moreover, this mechanism agrees with the work of [25], who have shown that the inductive loop of impedance diagrams is due to an adsorption process.

The capacitive loops sizes, out of phase concerning the real axis, increased with higher AS C. R_p values, determined from the medium frequency limits on the Nyquist diagrams, confirmed a satisfactory protective capacity at 1 g/L AS. The metal/electrolyte interface modeling was carried out through an equivalent electrical circuit (Fig. 5).

Two equivalent circuits were applied using a Bouckamp program. As shown in Fig. 5, the capacitor was substituted through a CPE, which offered a different frequency response. CPE impedance is represented by the following equation [26]:

$$Z_{CPE}(\omega) = Q^{-1}(j\omega)^{-n} \tag{12}$$

where Q is a constant in $\Omega/\text{cm}^{-2}/\text{s}^n$, ω is the angular frequency in rad/s^{-1} and n is CPE exponent ($-1 < n < 1$). Z_{CPE} can represent either an inductance, or a Warburg impedance, or a capacitance or a resistance ($n = -1, 0$ and 0.5 , respectively). The following elements from the suggested equivalent circuits are: $R_s, R_f, R_{ct}, n_f, n_{ct}, CPE_f$ and CPE_{dl} .

R_p was calculated by the following equation:

$$R_p = R_f + R_{ct} \tag{13}$$

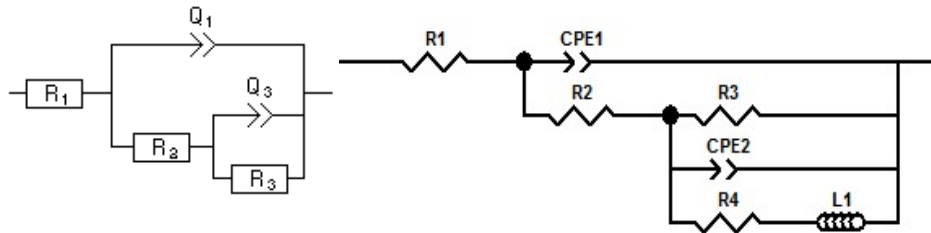


Figure 5. Equivalent circuit model used for fitting experimental EIS data.

Electrochemical parameters and IE(%) values, for different AS C, obtained by EIS, and using the equivalent circuit, are given in Table 3.

Table 3. Impedance parameters for AA in a 3.5 %NaCl solution without and with AS.

Medium	C g/L	R_s Ω/cm^2	Q_f $\Omega^{-1}/\text{S}^n/\text{cm}^2$	n_f	R_f Ω/cm^2	Q_{ct} $\Omega^{-1}/\text{S}^n/\text{cm}^2$	n_{ct}	R_{ct} Ω/cm^2	R_p Ω/cm^2	R_L Ω/cm^2	L (H)	IE(%)
Blank	-	12.5±0.3	170.3±0.12	1	107±0.2	-	-	1111.0±2.4	1218	16.0±1.3	211	-
AS	0.25	5.0±0.1	72.1±0.23	0.885	879±0.3	130.8±0.31	0.575	1039.0±5.3	1918	1550.0±4.3	193	36.5
	0.50	4.5±0.2	44.8±0.34	0.805	275±0.6	66.9±0.45	0.525	2093.0±6.1	2360	2080.0±7.3	314	48.5
	0.75	4.0±0.3	66.4±0.13	0.856	619±0.4	150.6±0.72	0.687	1879.0±5.2	2498	2140.0±5.3	351	51.2
	1.00	4.6±0.1	12.7±0.15	0.739	4542±0.1	16.7±0.53	0.948	4426.0±3.4	8968	7948.0±2.3	505	86.4

From the obtained parameters, it can be seen that AS addition decreased Q_{ct} and Q_f values and increased R_{ct} and R_f . The significant decrease in the capacitance values is often ascribed to a reduction in the dielectric constant or a rise in the double electric layer thickness, due to AS molecules adsorption onto the AA surface [27-29].

IE(%) and R_p values increased with AS addition, indicating the formation of an insulated adsorption layer. This phenomenon suggests that the charge transfer process was impeded when the uncovered area available for this process decreased, which can be explained by AS molecules adsorption at the metal/electrolyte interface [30].

T effect

Polarization curves

In general, T has a remarkable effect on corrosion phenomena. CR increases when the test T increases, which induces changes in the inhibitors action [31, 32]. PDP study of AA in NaCl without and with AS (1 g/L), at T from 298 to 328 K, was herein conducted. The corresponding obtained PDP curves are shown in Fig. 6.

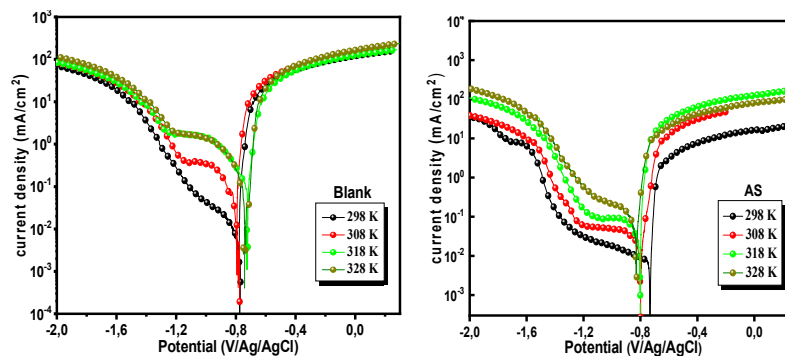


Figure 6. PDP curves for AA in in NaCl without and with 1 g/L AS, at different T.

J was higher with an increase in T from 298 to 328 K. The curves of the cathode and anode were consistent with an equivalent mechanism within the whole T range. AA E_{corr} was little modified by the increase in T to 328 K, in 3.5% NaCl without and with AS.

E_{corr} , i_{corr} , β_c and IE(%) values are summarized in Table 4. In general, throughout the studied range, T higher values caused an increase in i_{corr} . The i_{corr} evolution in only 3.5% NaCl confirmed an increasing metallic dissolution with higher T. Nevertheless, the rise in i_{corr} with higher T, in AA presence, was much smaller than in the uninhibited solution. These results confirm and complement those obtained by EIS. AS showed better (IE%) in the studied T range (308, 318 and 328 K).

Table 4. AA electrochemical parameters in 3.5 % NaCl with and without AS, at different T.

Medium	T (K)	E_{corr} (mV/Ag/AgCl)	i_{corr} (μ A/cm ²)	β_c (mV/dec ⁻¹)	β_a (mV/dec ⁻¹)	IE(%)
Blank	298	774	10.8	359	216	-
	308	773	76.7	302	157	-
	318	716	143.6	235	186	-
	328	731	171.1	247	182	-
AS	298	733	1.4	293	155	87.0
	308	796	10.9	274	151	85.7
	318	796	23.2	286	144	83.8
	328	823	32.9	290	159	80.7

Thermodynamic studies

The Arrhenius-type dependence observed between i_{corr} and T allowed to calculate the corrosion process E_a value at different T, in AS absence and presence.

Fig. 7 illustrates the i_{corr} logarithm (L_nCR) variation as a function of the absolute T inverse (1/T). This $L_n i_{corr} = f(1/T)$ variation was linear for different C of both uninhibited and inhibited media. From the Arrhenius relation 7, we can calculate E_a for different C of the solutions without and with AS [33-35].

$$Ln(i_{cor}) = Ln(K) - \frac{Ea}{RT} \tag{14}$$

where R is the universal gas constant and K is the Arrhenius pre-exponential constant. The values collected from the slope of the linear plots are presented in Table 5, where it is seen that E_a value for the studied AS C was higher than that of the uninhibited solution. The increased E_a in AS presence may also be interpreted as physical adsorption.

Indeed, an enormous energy barrier within the inhibited solution was associated with physical adsorption or weak chemical bonding of AS with the AA surface [36, 37]. An alternative formula of the Arrhenius equation allows ΔH_a and ΔS_a determination, according to the following equation (15):

$$I_{corr} = \frac{RT}{Nh} \exp\left(\frac{\Delta S_a}{R}\right) \exp\left(-\frac{\Delta H_a}{RT}\right) \tag{15}$$

where N is Avogadro’s number and h is Plank’s constant.

Fig. 6 illustrates $L_n (i_{corr}/T)$ variation as a function of the inverse $T (1/T)$. The obtained lines have a slope equal to $-\Delta H_a/R$, and an ordinate at the origin equal to $L_n (R/Nh) + (\Delta S_a/R)$. From these equations, we can therefore calculate ΔH_a and ΔS_a values, which are given in Table 5.

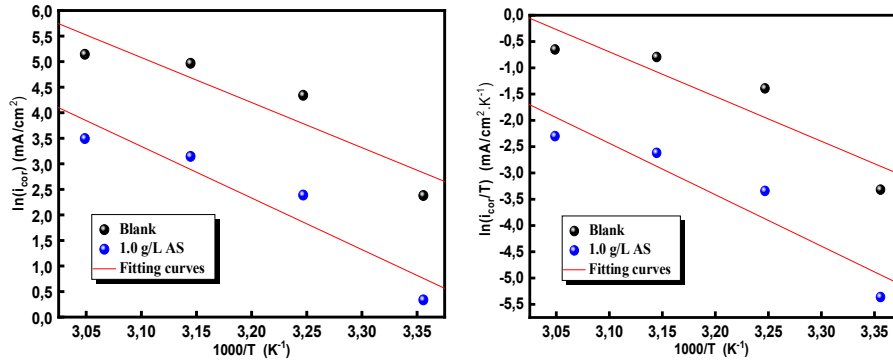


Figure 7. AA Arrhenius plots without and with 1 g/L AS.

Table 5. E_a , ΔH_a and ΔS_a values for AA in NaCl without and with AS.

Medium	E_a kJ/mol	ΔH_a kJ/mol	ΔS_a J/mol.K
Blank	73.3	70.7	15.9
1 g/L	83.9	81.3	34.4

ΔH_a positive signs reflect the endothermic nature of the AA dissolution process. Indeed, increased ΔH_a , in AS presence, corresponds to a decrease in AA dissolution [38]. Additionally, Table 5 shows that ΔS_a value was higher in AS presence than in its absence, which suggests that a rise in disorder occurred during the transition from the reactant to the activated complex, during the corrosion process [39, 40].

SEM

The surface morphologies of AA samples, in 3.5% NaCl without and with AS, were analyzed by SEM. The surface compositions were determined from their EDX spectra. Figs. 8 and 9 show SEM-EDX of AA corroded and inhibited surfaces, after 2 h of immersion in 3.5% NaCl. SEM image of AA surface in 3.5% NaCl without AS (Fig. 8) shows the extreme degradation around the intermetallic particles.

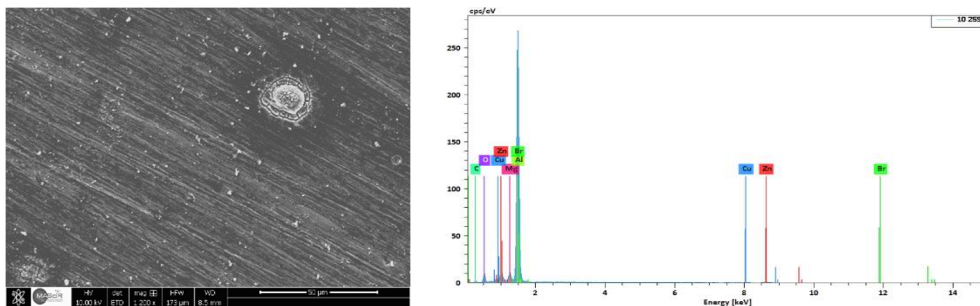


Figure 8. Surface morphology and EDX of AA after immersion for 2 h in NaCl without AS.

Fig. 10 shows SEM-EDX of AA surface, after 20 h immersion in 3.5% NaCl with AS. In AS presence (Fig. 9 and 10), the AA matrix almost did not suffer corrosion attack by NaCl. This is in accordance with AS higher corrosion IE(%), as observed from electrochemical measurements.

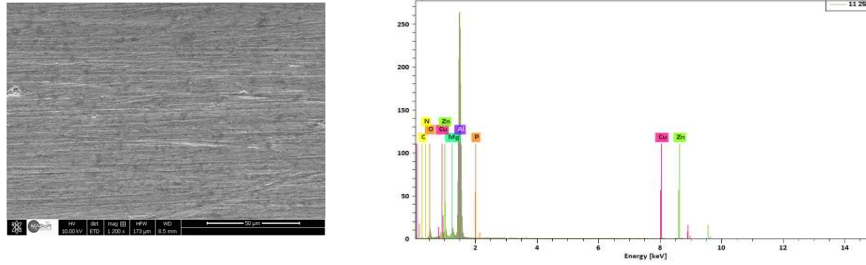


Figure 9. Surface morphology and EDX of AA after 2 h immersion in 3.5% NaCl with 1g/L AS.

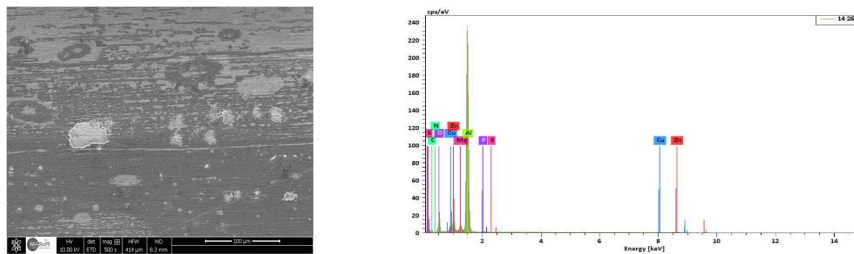


Figure 10. Surface morphology and EDX of AA after 20 h immersion in 3.5% NaCl with 1 g/L AS.

EDX analysis of the corrosion products created on the AA surfaces is presented in Table 6. P, N and S peaks appearance designate that the minority of AS were adsorbed onto the AA. P appearance is associated to the presence of diverse bioactive compounds comprising vitamins (A, C, E and B (vitamin B1) [8] and minerals (P, Ca, Zn, K, Na, Fe and Cu) [17]. Therefore, these results confirm those attained from electrochemical measurements.

Table 6. EDX analysis of the corrosion products created on the AA surface.

Element	Blank	AS (2 h)	AS (20 h)
C	9.40	9.55	18.51
N	-	0.39	1.54
O	16.70	12.86	24.43
Mg	2.19	2.65	1.65
Al	53.01	72.24	51.25
P	-	0.02	0.25
S	-	-	0.02
Cu	0.49	0.37	0.52
Zn	2.52	1.91	1.82

AFM

AFM allowed knowing electrochemical interactions at the nanometric, or even atomic, scale. It is an essential tool for the study of interface phenomena, such as corrosion [41-44]. Micrographs of the AA surface without and with AS (1 g/L) are presented in three dimensions (Fig. 11).

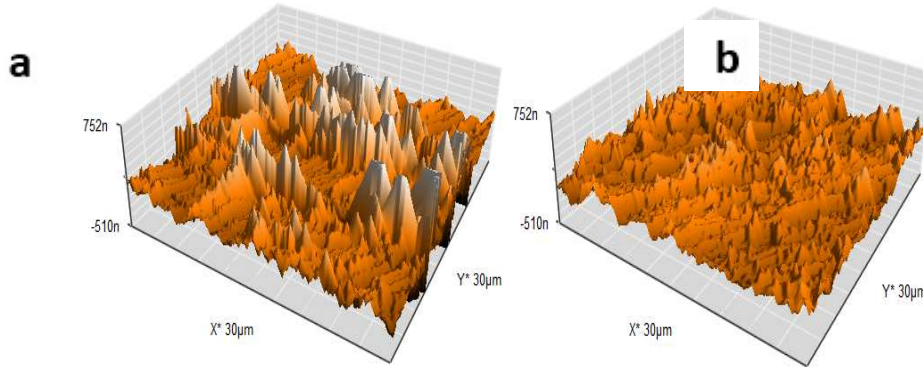


Figure 11. 3D AFM images of AA after 24 h immersion in NaCl: (a) without and (b) with 1 g/L AS.

Fig. 11a shows that the AA surface in 3.5% NaCl without AS suffered severe damage, while with it, R_a was significantly reduced (Fig. 12).

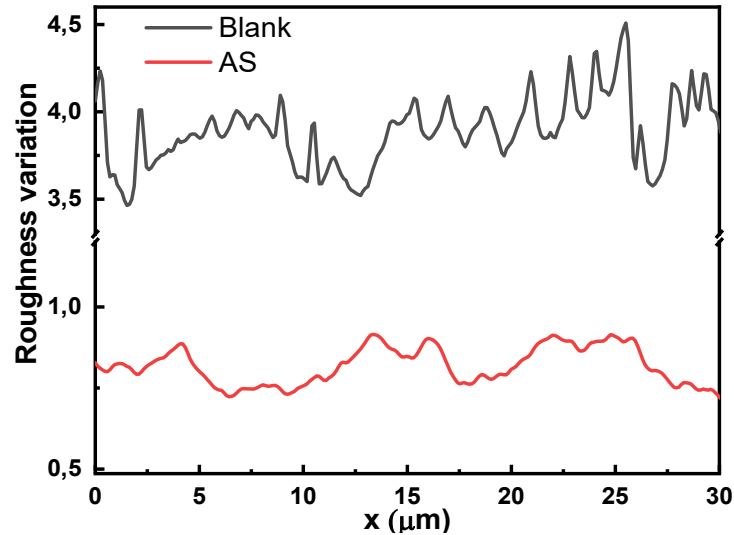


Figure 12. R_a variation of AA after 24 h immersion in NaCl without and with AS (1 g/L).

R_a of the AA surface immersed in 3.5% NaCl without and with AS was 338.17 and 79.3 μm , respectively. R_a reduction confirmed the formation of a film by AS, which covered the entire AA surface (Table 7).

Table 7. R_a and S_a values derived from AFM.

	AA (3.5%NaCl)	AA (3.5% NaCl + 1 g/L AS)
R_a (μm)	338.17	79.3
S_a (nm)	104.5	76.47

X-RD analysis

X-RD has been performed for determining the products developed on the AA surface. AA X-RD patterns, after 20 h immersion in NaCl without and with AS (1 g/L), are displayed in Fig. 13.

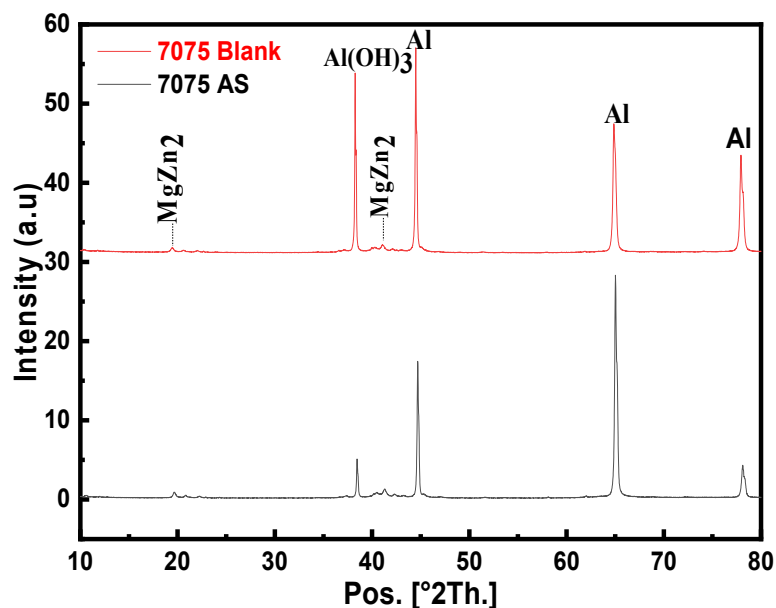


Figure 13. X-RD patterns of AA in NaCl without and with 1 g/L AS.

X-RD patterns determined three significant peaks: the one from Al was the strongest; the $MgZn_2$ precipitate peak was very weak; and the intensity of that from $Al(OH)_3$ was reduced in AS presence, indicating that it protected the alloy [45-47]. There were some other AS compounds which X-RD could not identify. The theoretical studies would help us to illustrate it.

DFT calculations

After the experimental investigation was performed with AS, the theoretical study was executed to compare its components. GA and D-M have been theoretically examined through DFT calculations, for explaining the IE(%) structural parameters. Geometrical optimization structure, HOMO and LUMO, are presented in Fig. 14.

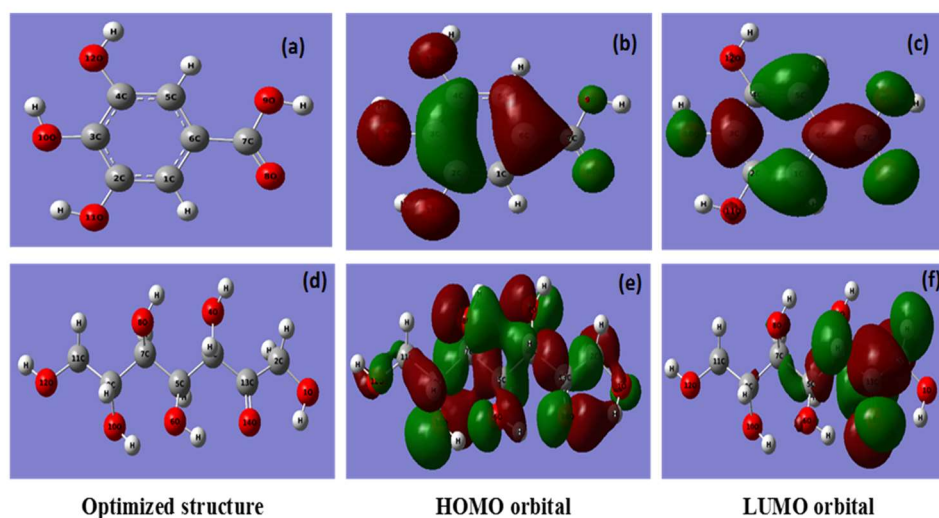


Figure 14. Geometrical optimization structure, HOMO and LUMO for GA (a, b, c) and D-M (d, e, f) at DFT/6-31G(d,p) in the aqueous phase.

It is seen that HOMO and LUMO electron density is distributed over GA molecule, indicating that it represents both nucleophilic and electrophilic centers from which the electron can be transferred from/to the AA vacant 3-d orbit. However, in D-M case, HOMO is distributed all over it, while LUMO is concentrated on the propanone group, which represents the electrophilic center that accepts electrons transferred by retrodonation from the AA surface.

Some quantum chemical descriptors, including ΔE , σ , η , χ and ΔN , in both gas and aqueous phases, were also quantified (Table 8). E_{HOMO} and E_{LUMO} refer to the tested compound electron donation and receiving ability to/from AA atomic orbitals. HOMO higher value indicates that AS have an excellent ability for donating electrons to the AA surface vacant d-orbitals.

In comparison, LUMO lower value implies that AS has an affinity for accepting electrons from the d-orbitals of the metal surface. It can be noticed from Table 8 that HOMO theoretical order in the gas and aqueous phases is GA > D-M, suggesting that the former had good electron-donating properties. ΔE is another fundamental descriptor that elucidates the inhibitor reactivity towards the metal surface. As ΔE diminishes, the inhibitor molecule reactivity is enhanced (higher IE) [48].

From Table 8, ΔE values obtained in both gas and aqueous phases follow the order D-M > GA, indicating that the latter has more reactivity than that of D-M.

Table 8. Various descriptors quantum chemical for GA and D-M molecules in both gas and aqueous phases.

Parameters	Gas phase		Aqueous phase	
E_{HOMO} (eV)	-7.403	-6.497	-7.354	-6.290
E_{LUMO} (eV)	-1.391	-1.699	-1.370	-1.429
ΔE_{gap} (eV)	6.011	4.798	5.983	4.860
η (eV)	3.005	2.399	2.991	2.430
σ (eV ⁻¹)	0.332	0.416	0.334	0.411
χ (eV)	4.397	4.098	4.362	3.860
ΔN	0.070	0.150	0.076	0.197
μ (D)	3.815	4.996	6.534	6.177

According to χ equalization principle [49], D-M with high χ reflected lower reactivity than that of GA. Based on literature [50, 51], it is known that an inhibitor molecule can donate its electron to a metallic surface if $\Delta N > 0$ and < 0 . However, ΔN order in the aqueous phase was GA (0.197) > D-M (0.076), suggesting that the former had higher ΔN towards the AA surface atoms than that of the latter. The present investigation showed that μ of GA and D-M did not have a significant order, and that the magnitudes of the mentioned descriptors for both molecules had the same trend in gas and aqueous phases. Consequently, these molecules, especially GA, may have been responsible for experimentally recorded AS IE(%).

Local reactivity descriptors (Fukui indices)

Fukui indices are important to recognize electrophilic and nucleophilic reactive centers within the same molecule [52]. Fig. 15 displays the graphical outcomes of

neutral GA and D-M molecules electrophilic/nucleophilic attacks, in terms of atom-condensed Fukui functions (Table 9) in the aqueous medium.

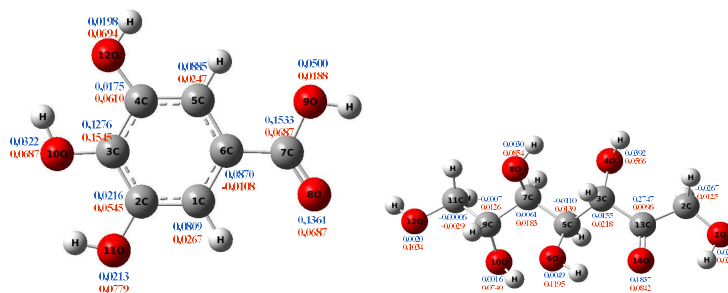


Figure 15. Schematic representation of Fukui indices f_k^+ (blue) and f_k^- (red) for the considered molecules in the aqueous medium.

Table 9. Fukui functions and their dual descriptors for the considered molecules in the aqueous medium.

Atoms	D-M			GA		
	f_k^+	f_k^-	f_k^2	f_k^+	f_k^-	f_k^2
C1	-	-	-	0.08091	0.02675	0.05416
C2	-0.02679	0.01255	-0.03934	0.02166	0.05458	-0.03292
C3	0.01557	0.02180	-0.00623	0.12769	0.15452	-0.02683
C4	-	-	-	0.01751	0.06100	-0.04349
C5	-0.01105	0.01397	-0.02502	0.08856	0.02472	0.06384
C6	-	-	-	0.08702	0.14052	-0.0535
C7	0.00618	0.01830	-0.01212	0.15336	-0.01086	0.16422
C9	-0.00072	0.01260	-0.01332	-	-	-
C10	-	-	-	-	-	-
C11	-0.00006	-0.00294	0.00288	-	-	-
C12	-	-	-	-	-	-
C13	0.27468	0.00967	0.26501	-	-	-
O1	0.02303	0.02221	0.00082	-	-	-
O4	0.03929	0.05665	-0.01736	-	-	-
O6	0.00493	0.11951	-0.11458	-	-	-
O8	0.00301	0.08545	-0.08244	0.13612	0.06878	0.06734
O9	-	-	-	0.05005	0.01882	0.03123
O10	0.00164	0.07402	-0.07238	0.03228	0.14597	-0.11369
O11	-	-	-	0.02136	0.07795	-0.05659
O12	0.00202	0.10349	-0.10147	0.01989	0.06944	-0.04955
O14	0.18375	0.08428	0.09947	-	-	-

According to the schematic representation of Fukui indices, it is visible that almost all the GA molecule atoms interacted, as electrophilic and nucleophilic sites, i.e., higher values of f_k^+ and f_k^- were obtained. However, in D-M molecule case, C(13), O(14), O(4) and O(1) acted as major locations for nucleophilic behavior, and all its O atoms acted as major centers, with electrophilic conduct.

Fukui functions second order (f_k^2), also called dual descriptor, provides an easy and intuitive approach to chemical reactivity [53], and it can be evaluated using the following equation (16):

$$f_k^2 = f_k^+ - f_k^- \quad (16)$$

Fukui functions and their dual descriptors are shown in Fig.16.

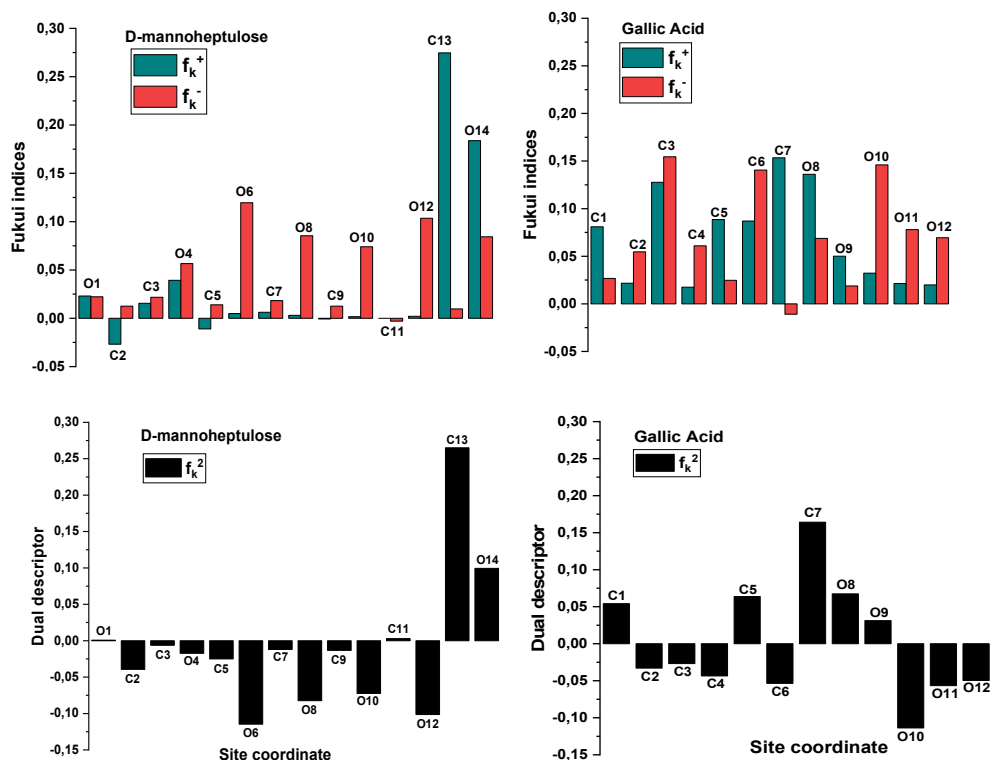


Figure 16. Graphical representation of Fukui functions and their dual descriptors.

It was reported that if $f_k^2 < 0$, it will tend to transfer electrons to the metal surface, while if $f_k^2 > 0$, it will accept electrons from the metal [54]. As shown in Table 9 and Fig. 16, the most active sites for D-M and GA electron-accepting centers had the following sequence: C(13) > O(14) > C(11) > O(1) and C(7) > O(8) > C(5) > C(1) > O(9), respectively. However, the most active sites for D-M and GA donating active centers followed the order: O(6) > O(12) > O(8) > O(10) > C(2) > C(5) > O(4) > C(9) > C(7) > C(3) and O(10) > O(11) > C(6) > O(12) > C(4) > C(2) > C(3), respectively.

Conclusions

Electrochemical, thermodynamic, surface analysis and theoretical studies were used to characterize AS IE(%) on AA corrosion in a 3.5% NaCl solution. The following conclusions were drawn from this study:

- AS were an excellent green corrosion inhibitor for AA in a neutral 3.5% NaCl medium.
- AS IE(%) measured by EIS reached up 87% at 1 g/L inhibitor C.
- Polarization curves showed that AS is a mixed type inhibitor.
- AS adsorption onto the AA surface followed Langmuir's isotherm. Thermodynamic parameters showed that AS was highly adsorbed onto the AA surface.
- The study of the AA surface morphology and roughness by SEM/EDX and AFM showed a stable and insoluble adherent deposit.

- Theoretical calculations showed that there was a correlation between AS molecular structure and its IE(%). They suggest that the effectiveness of AS Pc constituents studied through DFT pursued the sequence: GA > D-M.

Authors' contributions

M. Radi: wrote the paper. **R. Melian:** conceived and designed the analysis. **M. Galai:** collected the data. **N. Dkhirche:** performed the analysis. **E. Ech-chihbi:** performed the analysis. **M. Ebn Touhami:** conceived and designed the analysis.

Abbreviations

AA: 7075-T6 Al alloy

AC: alternating current

AFM: atomic force microscope

AgCl: silver chloride

Al₂Cu: aluminum bronze

Al₃Fe: iron aluminide

AS: avocado seeds

ATR: attenuated total reflection mode

C: concentration

CE: counter electrode

CPE: constant phase element

CR: corrosion rate

DFT: density functional theory

DM: D-mannoheptulose

E: potential

E_a: activation energy

E_{corr}: corrosion potential

EDX: energy dispersive X-ray

E_{HOMO}: energy of the highest occupied molecular orbital

EIS: electrochemical impedance spectroscopy

E_{HOMO}: energy of the highest unoccupied molecular orbital

E_{LUMO}: energy of the lowest unoccupied molecular orbital

E_{ocp}: circuit potential evolution

FTIR: Fourier transform infrared spectroscopy

GA: gallic acid

i_{corr}: corrosion current density

IE(%): inhibition efficiency

IEFPCM: integral equation formalism variant of the polarizable continuum model

J: current density

KBr: potassium bromide

L: inductance

Mg₂Si: magnesium silicide

MgZn₂: dizinc magnesium

MPA: Mulliken population analysis

NaCl: sodium chloride

OCP: open circuit potential

Pc: phytochemicals

PDP: potentiodynamic polarization

Psi: pound-force per square inch
Q_c: double layer capacitance of the inhibitors film
Q_{ct}: Al double layer capacitance
R_a: average roughness
R_{ct}: charge transfer resistance
RE: reference electrode
R_L: resistance of the inductive loop
R_p: polarization resistance
S_a: average surface roughness
SEM: scanning electron microscopy
SR: scan rate
T: temperature
WE: working electrode
X-RD: X-ray diffraction

Symbols definition

β_a: anodic slope
β_c: cathodic slope
ΔE: energy gap between HOMO and LUMO
ΔH_a: enthalpy of activation.
ΔN: fraction of electrons transfer
ΔS_a: entropy of activation
η: global hardness
μ: dipole moment
φ: function work
σ: global softness
χ: electronegativity

References

1. Polmear J. Light Alloys-Metallurgy of the Light Metals. Mater Sci Appl. 1995;2.
2. Meng Q, Frankel GS. Effect of Cu Content on Corrosion Behavior of 7xxx Series Aluminum Alloys. J Electrochem Soc. 2004;151;271. <https://doi.org/10.1149/1.1695385>
3. Birbilis N, Cavanaugh MK et al. Proceedings of Symposium: Application of Materials Science to Military Systems. J Mater Sci Technol. 2006;4;115-126. <https://doi.org/10.1016/j.corsci.2006.02.007>
4. Mondolfo LF. The Aluminum-Magnesium-Zinc Alloys, Research and Development Center, Revere Copper and Brass Inc, Rome, NY;1967.
5. Ashassi-Sorkhabi H, Asghari E. Electrochemical corrosion behavior of Al7075 rotating disc electrode in neutral solution containing L-glutamine as a green inhibitor. J Appl Electrochem. 2010;40;631-637. <https://doi.org/10.1007/s10800-009-0038-5>
6. Obot IB, Obi-Egbi NO. An interesting and efficient green corrosion inhibitor for aluminum from extracts of *Chlomolaenaodorata L.* in acidic solution. J Appl Electrochem. 2010;40;1977-1984. <https://doi.org/10.1007/s10800-010-0175-x>

7. Rafiquee MZ, Sadaf K, Saxena N et al. Investigation of some oleochemicals as green inhibitors on mild steel corrosion in sulfuric acid. *J Appl Electrochem.* 2009;39;1409-1417. <https://doi.org/10.1007/s10800-009-9811-8>
8. Mark L, Adrienne J. Hass Avocado Composition and Potential Health Effects. *Crit Rev Food Sci Nutr.* 2013;53;738-750. <https://doi.org/10.1080/10408398.2011.556759>
9. Mu GN. Synergistic inhibition between o-phenanthroline and chloride ion on cold rolled steel corrosion in phosphoric acid. *Mater Chem Phys.* 2004;86;59-68. <https://doi.org/10.1016/j.matchemphys.2004.01.041>
10. Singh A, Lin Y et al. Plant derived cationic dye as an effective corrosion inhibitor for 7075 aluminum alloy in 3.5% NaCl solution. *Int J Electrochem Sci.* 2014;9;55;60-5573. <https://doi.org/10.1016/j.jiec.2014.01.033>
11. Gerengi H. Anticorrosive Properties of Date Palm (*Phoenix Dactylifera L.*) Fruit Juice on 7075 Type Aluminum Alloy in 3.5% NaCl Solution. *Ind Eng Chem Res.* 2012;51;12835-12843. <https://doi.org/10.1021/ie301771u>
12. Ambrish S, Yuanhua L et al. Berberine as an Effective Corrosion Inhibitor for 7075 Aluminium Alloy in 3.5% NaCl Solution. *Int J Electrochem Sci.* 2014;9:5164-5176.
13. Bouckamp A. User's Manual Equivalent Circuit;1993;4:51.
14. Ech-chihbi E, Nahlé A et al. Computational, MD simulation, SEM/EDX and experimental studies for understanding adsorption of benzimidazole derivatives as corrosion inhibitors in 1.0 M HCl solution. *J Alloys Compd.* 2020;844;155842. <https://doi.org/10.1016/j.jallcom.2020.155842>
15. Paul K, Yadav M et al. Investigation on corrosion protection behavior and adsorption of carbonylhydrazide-pyrazole compounds on mild steel in 15% HCl solution: Electrochemical and computational approach. *J Mol Liq.* 2020;314;113513. <https://doi.org/10.1016/j.molliq.2020.113513>
16. El-Hajjaji F, Ech-chihbi E et al. Electrochemical and theoretical insights on the adsorption and corrosion inhibition of novel pyridinium-derived ionic liquids for mild steel in 1 M HCl. *J Mol Liq.* 2020;314;113737. <https://doi.org/10.1016/j.molliq.2020.113737>
17. Ouakki M, Galai M et al. Investigation of imidazole derivatives as corrosion inhibitors for mild steel in sulfuric acidic environment: experimental and theoretical studies. *Ionics.* 2020;6. <https://doi.org/10.1007/s11581-020-03643-0>
18. Saunois A, Baudouin C et al. Avocado flesh and/or skin extract rich in polyphenols and cosmetic, dermatological and nutraceutical compositions comprising same. *Brevet WO 2012/085224 A1.*
19. Kendig M, Davenport A et al. The mechanism of corrosion inhibition by chromate conversion coatings from X-ray absorption near edge spectroscopy (Xanes). *Corros Sci.* 1993;34;41-49. [https://doi.org/10.1016/0010-938X\(93\)90257-H](https://doi.org/10.1016/0010-938X(93)90257-H)
20. Kendig M, Jeanjaquet S et al. Role of hexavalent chromium in the inhibition of corrosion of aluminum alloys. *Surf Coat Tech.* 2001;140;58-66. [https://doi.org/10.1016/S0257-8972\(01\)01099-4](https://doi.org/10.1016/S0257-8972(01)01099-4)
21. Zhao J, Xia L et al. Effects of chromate and chromate conversion coatings on corrosion of aluminum alloy 2024-T3. *Surf Coat Tech.* 2001;140;51-57. [https://doi.org/10.1016/S0257-8972\(01\)01003-9](https://doi.org/10.1016/S0257-8972(01)01003-9)
22. Epelboin I, Keddam M. Faradaic impedances, diffusion impedance and reaction impedance. *J Electrochem Soc.* 1970;117;1052-1056. <https://doi.org/10.1149/1.2407718>
23. Epelboin I, Keddam M et al. Faradaic impedances and intermediates in electrochemical reactions. *Farad Disc Chem Soc.* 1973;56;264-273. <https://doi.org/10.1039/DC9735600264>

24. Epelboin I, Wiart R. Mechanism of the electrocrystallization of nickel and cobalt in acidic solution. *J Electrochem Soc.* 1971;118;1577-1582. <https://doi.org/10.1149/1.2407788>
25. Aoki I V, Bernard M et al. AC impedance and raman spectroscopy study of the electrochemical behaviour of pure aluminum in citric acid media. *Electrochim Acta.* 2001;46;1871-1878. [https://doi.org/10.1016/S0013-4686\(01\)00431-5](https://doi.org/10.1016/S0013-4686(01)00431-5)
26. Abdel-Gaber AM, Abd-El-Nabey BA et al. *Corros Sci.* 2009;51;1038-1042. <https://doi.org/10.1016/j.corsci.2009.03.003>
27. Popova A, Sokolova E et al. *Corros Sci.* 2003;45;33-58. [https://doi.org/10.1016/S0010-938X\(02\)00072-0](https://doi.org/10.1016/S0010-938X(02)00072-0)
28. Hsissou R, Benhiba F et al. New epoxy composite polymers as a potential anticorrosive coating for carbon steel in 3.5% NaCl solution: Experimental and computational approaches. *Chem Data Collec.* 2021;31;2405-8300. <https://doi.org/10.1016/j.cdc.2020.100619>
29. Hsissou R, Benhiba F et al. Performance of curing epoxy resin as potential anticorrosive coating for carbon steel in 3.5% NaCl medium: Combining experimental and computational approaches. *Chem Phys Lett.* 2021;783:0009-2614. <https://doi.org/10.1016/j.cplett.2021.139081>
30. Kassou O. Comparative study of low carbon steel corrosion inhibition in 200 ppm NaCl by amino acid compounds. *J Mater Environ Sci.* 2015;6;1147-1155.
31. Bommersbach P, Dumont-alemany C et al. Electrochemical Characterization of a corrosion inhibitor: influence of temperature on the inhibition mechanism. In: 207th Meeting of the Electrochemical Society. 2005.
32. Bommersbach P, Dumont-Alemany C et al. Formation and behaviour study of an environment- friendly corrosion inhibitor by electrochemical methods. *Electrochim Acta.* 2005. <https://doi.org/10.1016/j.electacta.2005.06.001>
33. El Hezzat M, Assouag M et al. Correlated DFT and electrochemical study on inhibition behavior of ethyl 6- amino-5-cyano-2-methyl-4-(p-tolyl)-4H-pyran-3-carboxylate for the corrosion of mild steel in HCl. *Der Pharma Chem.* 2015;10;77-88.
34. Ekanem UF, Umoren SA et al. Inhibition of mild steel corrosion in HCl using pineapple leaves (*Ananas comosus L.*) extract. *J Matt Sci.* 2010;45;5558-5566. <https://doi.org/10.1007/s10853-010-4617-y>
35. Ahamad I, Prasad R et al. Thermodynamic, Electrochemical and Quantum Chemical Investigation of Some Schiff Bases as Corrosion Inhibitors for Mild Steel in Hydrochloric Acid Solutions. *Corros Sci.* 2010;52;933-942. <https://doi.org/10.1016/j.corsci.2009.11.016>
36. Popova A, Sokolova E et al. AC and DC study of the temperature effect on mild steel corrosion in acid media in the presence of benzimidazole derivatives. *Corros Sci.* 2003;45;33-58. [https://doi.org/10.1016/S0010-938X\(02\)00072-0](https://doi.org/10.1016/S0010-938X(02)00072-0)
37. Elayyachy M, Elkodadi M et al. New bipyrazole derivatives as corrosion inhibitors for steel in hydrochloric acid solutions. *Mater Chem Phys.* 2005;93;281-285. <https://doi.org/10.1016/j.matchemphys.2005.03.059>
38. Guan NM, Xueming L et al. Synergistic inhibition between o-phenanthroline and chloride ion on cold rolled steel corrosion in phosphoric acid. *Mater Chem Phys.* 2004;86;59-68. <https://doi.org/10.1016/j.matchemphys.2004.01.041>
39. Singh AK, Quraishi MA. Investigation of the effect of disulfiram on corrosion of mild steel in hydrochloric acid solution. *Corros Sci.* 2011;53;1288-1297. <https://doi.org/10.1016/j.corsci.2011.01.002>

40. Singh AK, Shukla SK et al. Inhibitive effect of ceftazidime on corrosion of mild steel in hydrochloric acid solution. *Mater Chem Phys.* 2011;129;68-76. <https://doi.org/10.1016/j.matchemphys.2011.03.054>
41. Suzuki T, Nishihara H et al. *Corros Sci.* 1996;38;1223-1234. [https://doi.org/10.1016/0010-938X\(95\)00172-G](https://doi.org/10.1016/0010-938X(95)00172-G)
42. Nabel A, Mohamed N et al. Corrosion inhibition efficiency of nonionic Schiff base amphiphiles of p-aminobenzoic acid for aluminum in 4 N HCl. *Collo Surf A.* 2008;322;97-102. <https://doi.org/10.1016/j.colsurfa.2008.02.027>
43. Guan NM, Xueming L et al. *Mater Chem Phys.* 2004;86.
44. Singh AK, Quraishi MA. Investigation of the effect of disulfiram on corrosion of mild steel in hydrochloric acid solution. *Corros Sci.* 2011;53;1288-1297. <https://doi.org/10.1016/j.corsci.2011.01.002>
45. Wu Y, Zhang Y et al. Orange peel extracts as biodegradable corrosion inhibitor for magnesium alloy in NaCl solution: Experimental and theoretical studies. *J Taiwan Instit Chem Eng.* 2020;1-12. <https://doi.org/10.1016/j.jtice.2020.10.010>
46. Su H, Wang L et al. Insight into inhibition behavior of novel ionic liquids for magnesium alloy in NaCl solution: Experimental and theoretical investigation. *J Corros Sci.* 2019. <https://doi.org/10.1016/j.corsci.2019.108410>
47. Radi M, Melian R et al. Pumpkin seeds as an eco-friendly corrosion inhibitor for 7075-T6 alloy in 3.5% NaCl solution: Electrochemical, surface and computational studies. *J Mol Liq.* 2021;337;0167-7322. <https://doi.org/10.1016/j.molliq.2021.116547>
48. Saha SK, Banerjee P. A theoretical approach to understand the inhibition mechanism of steel corrosion with two aminobenzonitrile inhibitors. *RSC Adv.* 2015;5;71120-71130. <https://doi.org/10.1039/C5RA15173B>
49. Geerlings P, De Proft F. Chemical reactivity as described by quantum chemical methods. *Int J Mol Sci.* 2002;3;276-309. <https://doi.org/10.3390/i3040276>
50. Bouoidina A, Ech-chihbi E et al. Anisole derivatives as sustainable-green inhibitors for mild steel corrosion in 1 M HCl: DFT and molecular dynamic simulations approach. *J Mol Liq.* 2021;324;115088. <https://doi.org/10.1016/j.molliq.2020.115088>
51. Galai M, Rbaa M et al. Chemically functionalized of 8-hydroxyquinoline derivatives as efficient corrosion inhibition for steel in 1 M HCl solution: Experimental and Theoretical studies. *Surf Interf.* 2020;21;100695. <https://doi.org/10.1016/j.surfin.2020.100695>
52. Obot IB, Macdonald D. Density functional theory (DFT) as a powerful tool for designing new organic corrosion inhibitors. Part 1: an overview. *Corros Sci.* 2015;99;1-30. <https://doi.org/10.1016/j.corsci.2015.01.037>
53. Geerlings P, Ayers AW et al. The Woodward-Hoffmann rules reinterpreted by conceptual density functional theory. *Accou Chem Res.* 2012;45;683-695. <https://doi.org/10.1016/j.corsci.2015.01.037>
54. Yang W, Parr RG. Hardness, softness, and the Fukui function in the electronic theory of metals and catalysis. *Proc Nat Acad Sci.* 1985;82;6723-6726. <https://doi.org/10.1073/pnas.82.20.6723>